

Optimization-Based Image Reconstruction Regularized with Inter-Spectral Structural Similarity for Limited-Angle Dual-Energy Cone-Beam CT

Junbo Peng¹, Tonghe Wang², Richard L. J. Qiu¹, Chih-Wei Chang¹, Justin Roper¹, David S. Yu¹,
Xiangyang Tang³ and Xiaofeng Yang^{1*}

¹Department of Radiation Oncology and Winship Cancer Institute, Emory University, Atlanta, GA
30322

²Department of Medical Physics, Memorial Sloan Kettering Cancer Center, New York, NY 10065

³Department of Radiology and Imaging Sciences and Winship Cancer Institute, Emory University, Atlanta, GA
30322

Email: xiaofeng.yang@emory.edu

Running title: Dual-Energy CBCT Imaging

Keywords: Dual-Energy CT, Cone-Beam CT, Optimization, Structural Similarity

Abstract

Background: Limited-angle (LA) dual-energy (DE) cone-beam CT (CBCT) is considered as a potential solution to achieve fast and low-dose DE imaging on current CBCT scanners without hardware modification. However, its clinical implementations are hindered by the challenging image reconstruction from LA projections. While optimization-based and deep learning-based methods have been proposed for image reconstruction, their utilization is limited by the requirement for X-ray spectra measurement or paired datasets for model training.

Purpose: This work aims to facilitate the clinical applications of fast and low-dose DECBCT by developing a practical solution for image reconstruction in LA-DECBCT.

Methods: An inter-spectral structural similarity-based regularization was integrated into the iterative image reconstruction in LA-DECBCT. By enforcing the similarity between the DE images, LA artifacts were efficiently reduced in the reconstructed DECBCT images. The proposed method was evaluated using four physical phantoms and three digital phantoms, demonstrating its efficacy in quantitative DECBCT imaging.

Results: In all the studies, the proposed method achieves accurate image reconstruction without visible residual artifacts from LA-DECBCT projection data. In the digital phantom study, the proposed method reduces the mean-absolute-error (MAE) from 419 to 14 HU for the High-energy CBCT and 591 to 20 HU for the low-energy CBCT.

Conclusions: The proposed method achieves accurate image reconstruction without the need for X-ray spectra measurement for optimization or paired datasets for model training, showing great practical value in clinical implementations of LA-DECBCT.

1. Introduction

Dual-energy (DE) CT, as an implementation of spectral CT, has found a variety of clinical applications, including virtual non-contrast imaging,¹⁻³ virtual monochromatic imaging,⁴ automatic bone removal,⁵ and iodine quantification.⁶ On the other hand, cone-beam CT (CBCT), using a flat-panel detector (FPD), is a volumetric imaging technique that plays a vital role in image-guided radiation therapy,⁷ surgery,⁸ and interventional procedures.⁹ Recently, integrating DE imaging with CBCT has attracted increasing attention. It has shown promise in various applications, such as contrast-enhanced lesion detection,¹⁰ angiography,¹¹ material classification,¹² and dose calculation for image-guided photon and proton therapy.¹³⁻¹⁵

However, the routine practice of DECBCT has been hindered due to the lack of a practical DECBCT implementation. Early efforts in DECBCT involved performing two separate scans at different tube voltages.¹² Besides the excessive radiation dose compared to a single-energy scan, the utility of this data acquisition scheme is hindered by the motion-induced spatial misregistration between the two scans because of the much slower CBCT gantry rotation than that of diagnostic CT due to patient safety considerations.¹⁶ To achieve DECBCT with data acquisition time and radiation dose comparable to the single-energy scans, techniques such as fast kVp-switching and dual-layer FPD have been investigated on CBCT systems.^{11,17-19} Nonetheless, the fast kVp-switching faces technical challenges due to instability in the rapid X-ray tube voltage modulation on current CBCT scanners,²⁰ and the dual-layer FPD suffers from limited DE spectral separation due to its physical structure.¹⁸ In short, despite the success of these two schemes in diagnostic DECT scanners, both of them require sophisticated hardware upgrades on existing onboard CBCT scanners and have not been commercialized yet.

It has been an active research area to achieve low-dose single-scan DE imaging on current scanners without significant hardware modifications since the introduction of the slow kVp-switching technique with prior image constrained compressed sensing (PICCS)-based image reconstruction.²¹ From the data acquisition perspective, the reported methods can be divided into spatial and temporal downsampling schemes. The spatial downsampling strategies install a reciprocating or static beam filter on the source or detector side to selectively alter the spectrum of X-ray photons in specific paths,^{16,20,22-25} generating spatially alternated high- and low-energy projection data in each projection view. Two common issues of these methods are partial filtration in the penumbra region and increased noise after the beam filtration. The temporal downsampling methods acquire DE projection data with alternating angular distribution via a slow kVp-switching scheme or a fast-rotating filter installed on the source side.^{21,26-30} Among all the proposed data acquisition schemes, limited-angle (LA) DECBCT is the most cost-effective and easy-to-implement solution in terms of hardware, and it is readily available for existing scanners.²⁷⁻²⁹ As a temporal downsampling strategy, LA-DECBCT requires no hardware modification and alters the tube voltage only once in the middle of the source trajectory, acquiring DE projection data within two complementary LA arcs. Besides, the spectral separation between the DE projection data in this scheme can be higher than that of the beam filter-based solutions. In brief, LA-DECBCT is an ideal candidate for practical DECBCT solutions on existing scanners.

One of the major challenges of LA-DECBCT is reconstruction artifacts. Optimization-based reconstruction algorithms and deep learning models have been proposed to address this issue. The optimization-based methods exploit constraints on the image directional-total-variation (DTV) of virtual monochromatic or material-specific images during the one-step material decomposition.^{29,31,32} Such iterative material decomposition algorithms require accurate measurement or estimation of DE X-ray spectra, which is challenging on current CBCT scanners. Furthermore, the optimization in these algorithms is computation-intensive due to the nonlinear data model in one-step material decomposition. Ignoring imaging physics, deep learning models directly learn the mapping from the acquired data to the desired data via supervised learning. The data restoration can be performed in the projection domain or the image domain. The projection-domain model translates the under-sampled DE projection data to the full-sampled data, which are used for subsequent analytical reconstruction.²⁸ The image-

domain model translates the directly reconstructed DECBCT images contaminated by LA artifacts to high-quality images without artifacts.²⁷ Despite the state-of-the-art performance of the deep learning-based methods, their clinical potential is significantly limited by the requirement of paired LA- and full-sampled DECBCT datasets for the supervised model training, which are unavailable in real patient datasets. In short, the clinical application of LA-DECBCT is hindered by the lack of a practical solution to the challenging image reconstruction.

In this study, we propose an efficient optimization-based image reconstruction method for LA-DECBCT to facilitate the clinical application of quantitative DECBCT. Recognizing the fact that the complete structural information is preserved in the projection data and the DE images share the same anatomical structures, we introduce an inter-spectral structural similarity-based regularization term into the iterative image reconstruction in LA-DECBCT. We demonstrate the feasibility of the proposed image reconstruction algorithm and evaluate its performance via a study of four physical phantoms and a study of three digital phantoms.

2. Materials and methods

2.1 Principles of iterative CT reconstruction

Iterative image reconstruction methods formulate the CT projection as a discretized linear model³³

$$\vec{b} = F\vec{\mu} \quad (1)$$

where $\vec{\mu}$ denotes the vectorized CT image, F is the system matrix representing the forward projection operator, and \vec{b} indicates the acquired projection data. $\vec{\mu}$ has a dimension of $N_{vox} \times 1$ where N_{vox} is the number of voxels in the CT image, F is in a size of $N_v N_d \times N_{vox}$ where N_v is the number of projection views and N_d is the number of detector pixels, and \vec{b} has a dimension of $N_v N_d \times 1$.

With a Gaussian noise assumption on the projection data, the maximum likelihood estimation (MLE) is equivalent to a least-square optimization problem

$$\min_{\vec{\mu}} \left\{ \frac{1}{N_v N_d} \|F\vec{\mu} - \vec{b}\|_2^2 + \mathcal{R}(\vec{\mu}) \right\} \quad (2)$$

s. t. $\vec{\mu} \geq \vec{0}$

where $\|\cdot\|_2^2$ is the ℓ_2 norm measuring the Eculidean distance, and $\mathcal{R}(\cdot)$ is an image prior-based regularization term. For example, total variation (TV) norm, $\|\cdot\|_{TV}$, is a common choice of $\mathcal{R}(\cdot)$ based on the piece-wise constant property of CT images.³⁴

2.2 Inter-spectral structural similarity-based iterative image reconstruction for LA-DECBCT

In LA-DECBCT, the high-kVp projection data are acquired within the first half of the view angular range, and the low-kVp projection data is acquired within the other half. Thus, the data acquisition in LA-DECBCT can be formulated as

$$\begin{cases} \vec{b}_H = F_H \vec{\mu}_H \\ \vec{b}_L = F_L \vec{\mu}_L \end{cases} \quad (3)$$

where $\vec{\mu}_{H,L}$ are the DECBCT images, $F_{H,L}$ represent the forward projection matrices in the high- and low-kVp scans, and $\vec{b}_{H,L}$ indicate the acquired high- and low-kVp projection data.

F_H and F_L are the top and bottom half of the system matrix in a conventional single-energy scan in Eq. (1), i.e.,

$$F = \begin{bmatrix} F_H \\ - \\ - \\ F_L \end{bmatrix} \quad (4)$$

The projection data $\vec{b}_{H,L}$ at each X-ray spectrum are angular-limited, leading to severe LA artifacts in the DECBCT images directly reconstructed from the acquired projection data.

The proposed iterative method for LA-DECBCT reconstruction is based on the fact that the complete anatomical information acquired in the mixed-spectra projection data and the anatomical structures are consistent between DECBCT images. Therefore, we introduce a structural similarity-based regularization term to suppress the LA artifacts during the iterative reconstruction:

$$\begin{aligned} \min_{\vec{\mu}_H, \vec{\mu}_L} & \left\{ \frac{1}{N_v N_d} [\|F_H \vec{\mu}_H - \vec{b}_H\|_2^2 + \|F_L \vec{\mu}_L - \vec{b}_L\|_2^2] \right. \\ & \left. + \lambda [1 - \text{SSIM}(\vec{\mu}_H, \vec{\mu}_L)] + \eta [\|\vec{\mu}_H\|_{TV} + \|\vec{\mu}_L\|_{TV}] \right\} \\ & \text{s. t. } \vec{\mu}_{H,L} \geq \vec{0} \end{aligned} \quad (5)$$

where λ and η are two user-defined weighting factors that balance the tradeoff between reconstruction data fidelity and image regularization. In Eq. (5), $\text{SSIM}(\cdot, \cdot)$ calculates the structural similarity index measurement (SSIM) between two input images by³⁵

$$\text{SSIM}(\vec{\mu}_H, \vec{\mu}_L) = \frac{(2\overline{\vec{\mu}_H \vec{\mu}_L} + C_1)(2\sigma_{H,L} + C_2)}{(\overline{\vec{\mu}_H}^2 + \overline{\vec{\mu}_L}^2 + C_1)(\sigma_H^2 + \sigma_L^2 + C_2)} \quad (6)$$

where $\overline{\vec{\mu}_H}$ and $\overline{\vec{\mu}_L}$ are the mean values of DECBCT, σ_H and σ_L are the standard deviations of DECBCT, $\sigma_{H,L}$ indicates the covariance between DECBCT, and $C_{1,2}$ are two constants associated with the dynamic range of DECBCT.

The incorporation of the SSIM regularization is the key to the success of LA artifact reduction in iterative DECBCT reconstruction, which is the major contribution of this work. The conventional TV norm regularization can also be involved in the proposed iterative reconstruction for noise suppression.

2.3 Evaluation

The performance of the proposed iterative method for image reconstruction in LA-DECBCT has been evaluated using the data of both physical and digital phantoms. The physical phantom data were acquired on two table-top CBCT systems, and the digital phantom data were simulated using the DECT images acquired on a Siemens TwinBeam scanner.

2.3.1 Physical phantom study

Due to the difficulty of raw data acquisition in the commercial scanners, we collected the DE projection data of four physical phantoms from two table-top CBCT systems.

A Catphan©600 phantom and an anthropomorphic head phantom #1 were scanned on one system. The geometry of the system was designed to match that of a Varian On-Board Imager (OBI) CBCT scanner on the TrueBeam radiation therapy machine. The source-to-detector distance (SDD) and the source-to-axis distance (SAD) are 1500 mm and 1000 mm, respectively. The FPD consists of 1024×768 pixels with a size of 0.388×0.388 mm². A collimator was installed on the X-ray tube to suppress photon scattering. Therefore, only the central row of detector pixels was used for image reconstruction. In the Catphan©600 phantom scan, the high- and low-energy data were acquired at X-ray tube voltages at 125 kVp and 75 kVp. In the head phantom #1 scan, the dual-energy separation was achieved by an additional copper (Cu) filter. In the low-energy data acquisition, the tube voltage

was set to 100 kVp. In the high-energy data acquisition, the tube voltage was unchanged, but a 0.4-mm Cu filter was installed on the exit window of the X-ray tube, leading to a higher mean photon energy after the filtration. For both phantom scans, a total of 655 projections were taken over 360° angular range. The LA-DECBCT data consists of 191 projection views out of 0° to 105° in the high-energy data and 191 views out of 105° to 210° in the low-energy data. The total angular range of 210° is based on the short scan protocol of a Varian OBI system.³⁶ The imaging parameters of these two phantom scans are summarized in Table I.

Table I. Imaging parameters in the LA-DECBCT scans of physical and digital phantoms.

	Physical Phantom Study				Digital Phantom Study
	Catphan©600	Head Phantom #1	Catphan©700	Head Phantom #2	
High-Energy Spectrum	125 kVp	110 kVp + 0.4-mm Cu	125 kVp + 0.2-mm Sn		120 kVp + 0.6-mm Sn
Low-Energy Spectrum	75 kVp	110 kVp	125 kVp		120 kVp + 0.05-mm Au
Reconstruction Volume	512×512×5				256×256×150
Voxel Size (mm ³)	0.5×0.5×0.5				1.0×1.0×1.0
SDD/SAD (mm)	1500/1000				
Detector Dimension	1024×10		1408×15		1024×768
Detector Pixel Size (mm ²)	0.388×0.388		0.308×0.308		0.388×0.388
High-Energy Projection Views	191 views out of 0° to 105°		175 views out of 0° to 105°		
Low-Energy Projection Views	191 views out of 105° to 210°		175 views out of 105° to 210°		

A Catphan©700 phantom and an anthropomorphic head phantom #2 were scanned on the other table-top system. The geometry was consistent with the first system, except for the use of an FPD consisting of 1408×1408 pixels with a size of 0.308×0.308 mm². A collimator was also installed for scattering suppression, and only the central detector row was used for image reconstruction. Similar to the scan of head phantom #1, the dual-energy spectral separation in these two phantom scans was achieved by a 0.2-mm tin (Sn) filter. 600 views were acquired over 360° angular range in these two scans. Therefore, the LA-DECBCT scan consists of 175 projections within a 105° angular range at each X-ray spectrum. The scanning parameters can be found in Table I.

Of note, in the scans of head phantom #1, Catphan©700 phantom, and head phantom #2, the DE spectral separation was achieved via beam filtration instead of different tube voltages. This is because the collected experimental data were originally acquired for other studies. The spectral separation in the digital phantom study is similar because of the hardware design of the Siemens TwinBeam scanner. In this work, we re-sorted and reused these data, which effectively preserved our research purpose.

2.3.2 Digital phantom study

The proposed method was further evaluated on three digital anthropomorphic phantoms based on DECT images of three H&N patients acquired on a Siemens TwinBeam DECT scanner at our institute. The tube voltage of the

scanner was fixed at 120 kVp. The high- and low-energy data were acquired using a 0.6-mm tin filter and a 0.05-mm gold (Au) filter, respectively. For each patient, a volume of $256 \times 256 \times 150$ with a voxel size of $1 \times 1 \times 1$ mm³ was selected for the simulated scan of LA-DECBCT.

First, the DECT images were converted from HU to linear attenuation coefficient (LAC) maps with the effective LACs of water at the high- and low-energy X-ray spectra, which were simulated using the Spektr toolbox.³⁷ Second, the LA-DECBCT scan was simulated based on the geometry of the OBI system in the physical phantom study, as listed in Table I. SDD and SID were 1500 and 1000 mm, and the FPD was 1024×768 with a pixel size of 0.388×0.388 mm². The first 175 projections within 0° to 105° were simulated using the high-energy CBCT volume, and the second 175 projections within 105° to 210° were simulated using the low-energy CBCT volume. The simulated forward projection was implemented using Siddon's ray-tracing algorithm.³⁸

2.3.3 Image quality metrics

Mean absolute error (MAE), peak signal-to-noise ratio (PSNR), and SSIM were calculated between the reconstructed DECBCT and the reference images to evaluate the quantitative image quality. Inter-spectral SSIM is calculated between the reconstructed DECBCT images to demonstrate the efficacy of the similarity-based regularization. For the phantom studies, the standard deviations of CT numbers within uniform regions-of-interest (ROIs) are measured to indicate the noise level.

2.4 Implementation details

All the experiments were implemented on an NVIDIA A100 GPU with a memory of 80 GB. The optimization of Eq. (5) was solved using an Adaptive Moment Estimation algorithm built in the PyTorch framework.³⁹ The step size was set to 0.001 in the physical phantom experiments and 0.1 in the digital phantom experiments. The first-order decay rate was 0.9, and the second-order decay rate was 0.999. The weighting factor of the SSIM term (λ) was set to 0.1 in all the experiments. The weighting factor of the TV term (η) was set to 0.1 in the physical phantom experiments and 0 in the digital phantom experiments.

The proposed method was compared with three other methods. The first directly performed Feldkamp-Davis-Kress (FDK) reconstruction using the LA-DECBCT projection data. The second one was to perform iterative image reconstruction without any regularization term,

$$\begin{aligned} \min_{\vec{\mu}_H, \vec{\mu}_L} \left\{ \frac{1}{N_v N_d} \left[\|F_H \vec{\mu}_H - \vec{b}_H\|_2^2 + \|F_L \vec{\mu}_L - \vec{b}_L\|_2^2 \right] \right\} \\ \text{s. t. } \vec{\mu}_{H,L} \geq \vec{0} \end{aligned} \quad (7)$$

The third comparison method was to perform the TV-regularized iterative reconstruction

$$\begin{aligned} \min_{\vec{\mu}_H, \vec{\mu}_L} \left\{ \frac{1}{N_v N_d} \left[\|F_H \vec{\mu}_H - \vec{b}_H\|_2^2 + \|F_L \vec{\mu}_L - \vec{b}_L\|_2^2 \right] + \eta [\|\vec{\mu}_H\|_{TV} + \|\vec{\mu}_L\|_{TV}] \right\} \\ \text{s. t. } \vec{\mu}_{H,L} \geq \vec{0} \end{aligned} \quad (8)$$

The reconstruction took 10 seconds in the phantom studies and 260 seconds in the digital phantom studies.

3. Results

3.1. Study of physical phantoms

Reconstructed DECBCT images of the Catphan©600 phantom and head phantom #1 are summarized in Figure 1. The reference DECBCT images were reconstructed from 360° projection data using the FDK algorithm.

Severe LA artifacts are observed in the results using FDK, iterative reconstruction, and TV-regularized iterative reconstruction. The proposed method without TV regularization achieves efficient LA artifact reduction, and no visible distortion is observed in the results. With additional TV regularization, the proposed method can further suppress the noise during the DECBCT reconstruction.

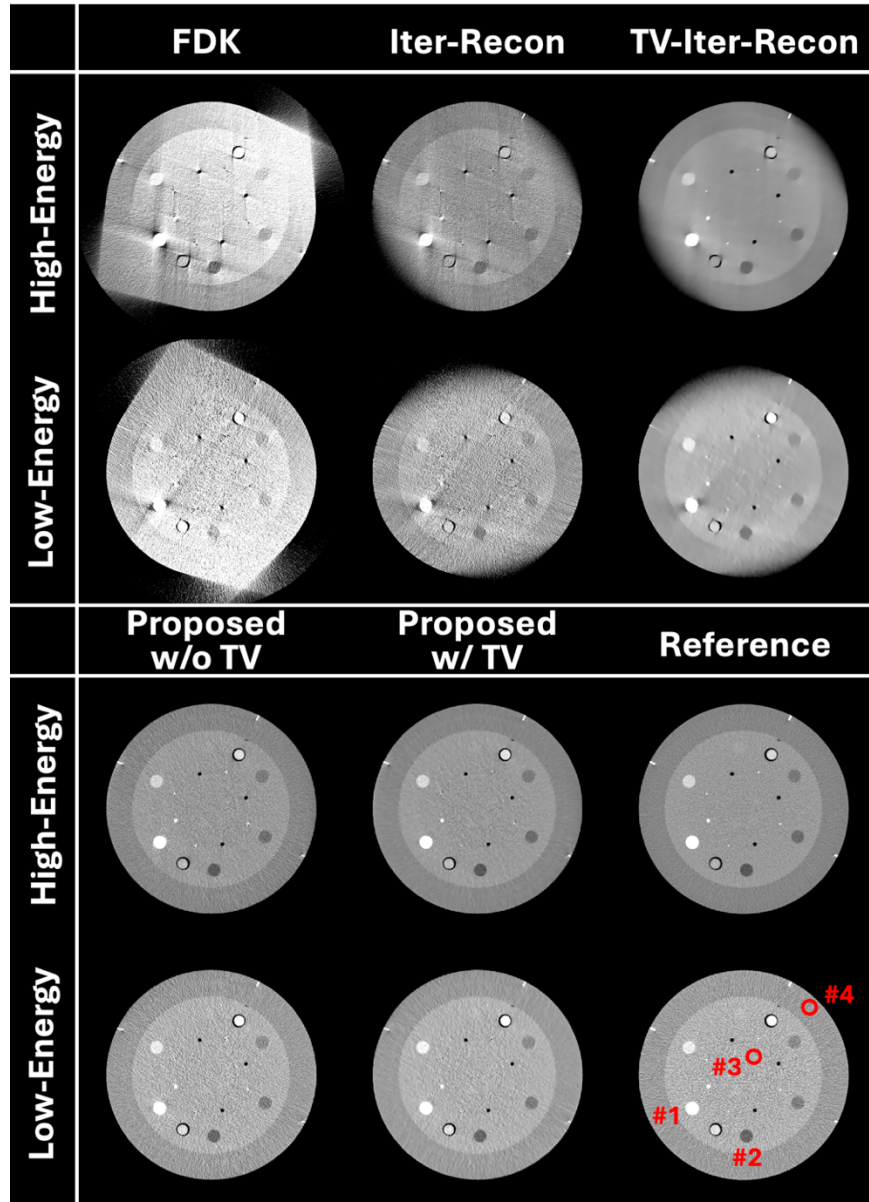


Figure 1. Reconstructed LA-DECBCT images of the Catphan©600 phantom using different methods. Display windows are [-750 -250] HU for the FDK results and [-500 500] HU for the other results.

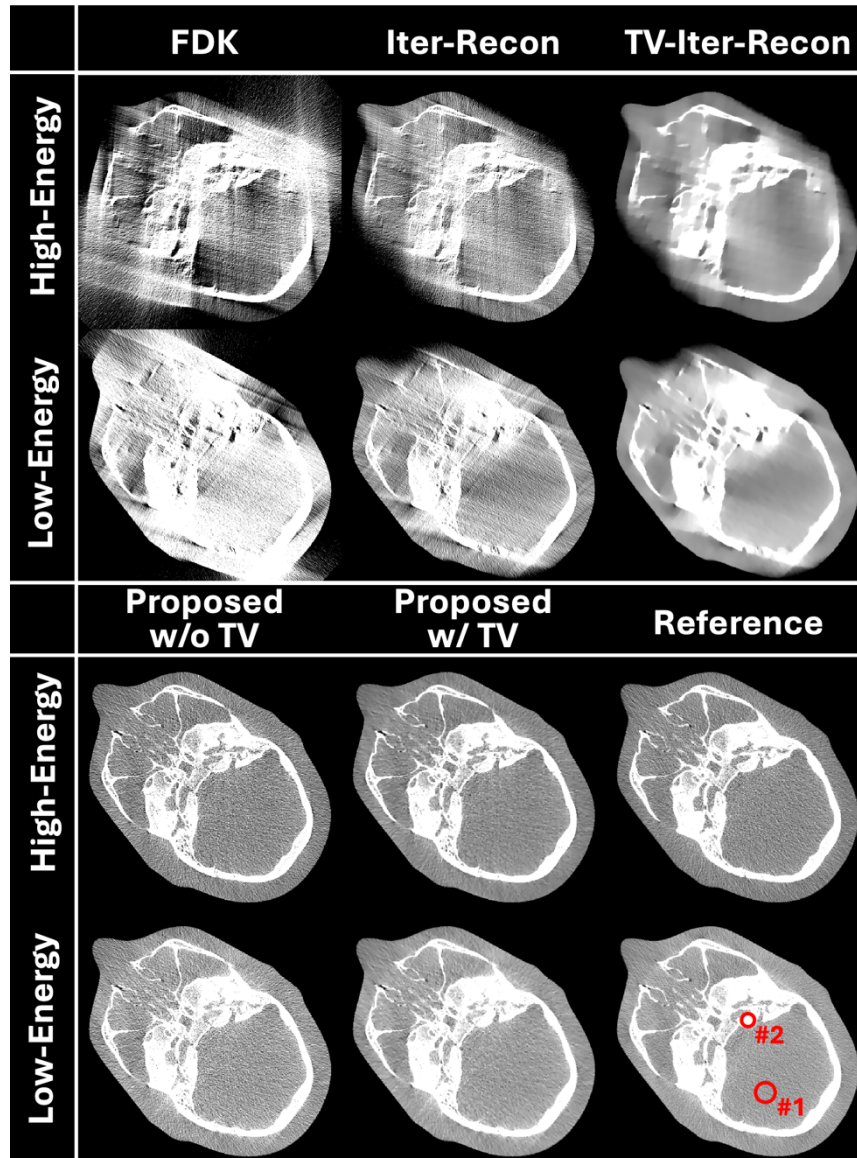


Figure 2. Reconstructed LA-DECBCT images of the anthropomorphic head phantom #1 using different methods. Display windows are $[-750 -250]$ HU for the FDK results and $[-500 500]$ HU for the other results.

Four ROIs in the Catphan©600 phantom and two in the head phantom #1 are selected to measure HU accuracy and noise level, as indicated in Figures 1 and 2. The results are summarized in Table II, showing that the proposed method can achieve accurate image reconstruction in LA-DECBCT, and the additional TV regularization further suppresses the noise level.

Table II. Mean and standard deviation of CT numbers (HU) measured within different ROIs which are indicated in Figures 1 and 2.

		Catphan©600				Head Phantom #1	
		#1	#2	#3	#4	#1	#2
High-Energy	Proposed w/o TV	916±71	-140±62	90±71	18±71	60±156	1557±220
	Proposed w/ TV	928±35	-153±16	92±39	18±12	61±65	1553±144

	Reference	916±53	-154±48	94±60	16±43	56±109	1539±200
Low-Energy	Proposed w/o TV	1169±136	-92±116	181±135	123±114	125±152	1767±211
	Proposed w/ TV	1179±67	-98±41	183±70	127±37	126±60	1744±140
	Reference	1174±128	-90±102	186±132	119±90	134±80	1787±123

PSNR and SSIM between the reconstructed LA-DECBCT images and reference images in these two phantom scans are summarized in Table III, where the proposed method gives the best performance over other compared methods. The inter-spectral SSIM between the reconstructed DE images is also included in Table III, showing that the proposed method maximizes the inter-spectral SSIM during the image reconstruction.

Table III. Quantitative metrics in the studies of Catphan©600 phantom and head phantom #1. The inter-spectral SSIM is calculated between reconstructed high- and low-energy images. Other results are calculated between the reconstructed and reference images.

			FDK	Iter-Recon	TV-Iter-Recon	Proposed w/o TV	Proposed w/ TV
Catphan©600	PSNR (dB)	High-Energy	42.65	51.91	54.07	55.33	56.58
		Low-Energy	41.47	47.97	51.23	51.32	52.37
	SSIM	High-Energy	0.84	0.97	0.98	0.99	0.99
		Low-Energy	0.83	0.97	0.98	0.99	0.99
		Inter-Spectral	0.74	0.98	0.98	1.00	1.00
Head Phantom #1	PSNR (dB)	High-Energy	38.48	45.65	47.07	49.96	52.01
		Low-Energy	39.61	45.97	47.35	50.01	52.51
	SSIM	High-Energy	0.73	0.96	0.97	0.99	0.99
		Low-Energy	0.81	0.97	0.98	0.99	1.00
		Inter-Spectral	0.61	0.94	0.96	1.00	1.00

Figures 3 and 4 summarize reconstructed DECBCT images of the Catphan©700 phantom and head phantom #2. The reference images were reconstructed from 360° projection data using the FDK algorithm. Consistent with previous results, LA artifacts are efficiently reduced by the proposed method and the noise can be further suppressed via the TV penalty.

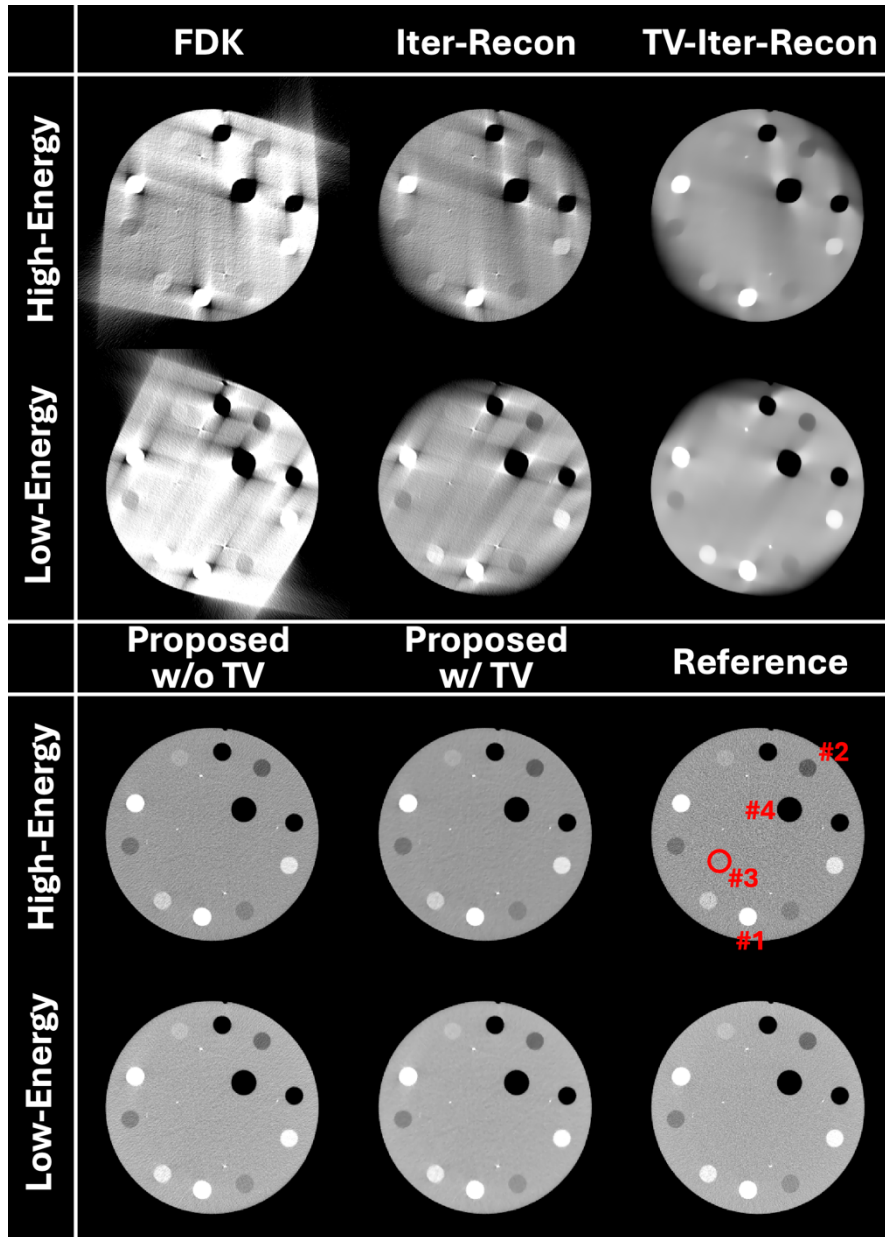


Figure 3. Reconstructed LA-DECBCCT images of the Catphan©700 phantom using different methods. Display windows are $[-750 -250]$ HU for the FDK results and $[-500 500]$ HU for the other results.

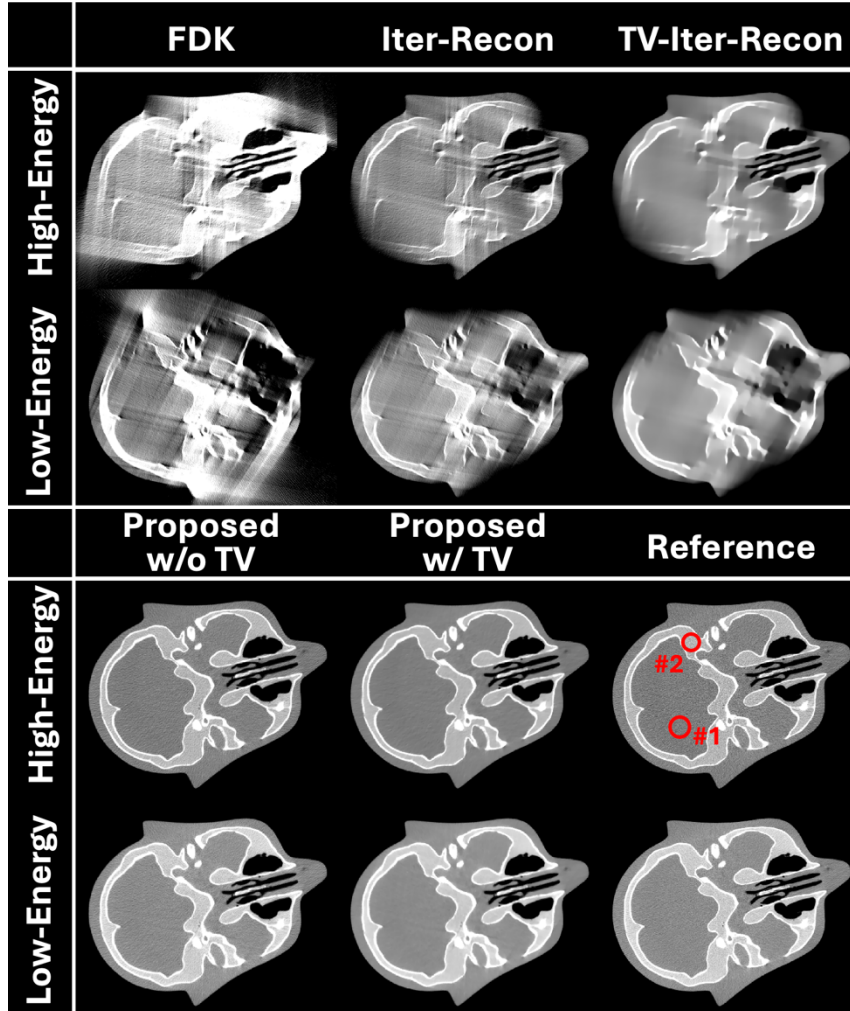


Figure 4. Reconstructed LA-DECBCT images of the anthropomorphic head phantom #2 using different methods. Display windows are $[-750 -250]$ HU for the FDK results and $[-500 500]$ HU for the other results.

The ROIs for HU accuracy and noise measurement are indicated in the reference high-energy images, and the results are listed in Table IV. The inter-spectral structural similarity-based regularization achieves accurate LA-DECBCT reconstruction, and the additional TV term performs noise suppression simultaneously.

Table IV. Mean and standard deviation of CT numbers (HU) measured within different ROIs which are indicated in Figures 3 and 4.

		Catphan©700				Head Phantom #2	
		#1	#2	#3	#4	#1	#2
High-Energy	Proposed w/o TV	1002±43	-137±43	101±44	-959±36	-13±45	211±41
	Proposed w/ TV	1001±15	-137±12	101±13	-959±11	-15±11	212±9
	Reference	1003±65	-136±58	104±70	-967±65	-14±67	209±71
Low-Energy	Proposed w/o TV	1206±41	-80±41	172±42	-952±36	46±42	300±40
	Proposed w/ TV	1206±16	-80±9	172±11	-953±10	45±8	302±9

	Reference	1207±46	-75±39	175±44	-947±36	41±52	301±53
--	-----------	---------	--------	--------	---------	-------	--------

Table V lists other quantitative metrics, including PSNR, SSIM, and inter-spectral SSIM, used in the study of Catphan©700 phantom and head phantom #2. Consistent with the previous two studies, the results of the proposed method show superior quantitative image quality over other results.

Table V. Quantitative metrics in the studies of Catphan©700 phantom and head phantom #2. The inter-spectral SSIM is calculated between reconstructed high- and low-energy images. Other results are calculated between the reconstructed and reference images.

			FDK	Iter-Recon	TV-Iter-Recon	Proposed w/o TV	Proposed w/ TV
Catphan©700	PSNR (dB)	High-Energy	41.58	52.50	52.80	60.46	60.07
		Low-Energy	41.23	52.25	52.88	62.30	63.11
	SSIM	High-Energy	0.79	0.98	0.99	1.00	1.00
		Low-Energy	0.80	0.98	0.99	1.00	1.00
		Inter-Spectral	0.59	0.97	0.98	1.00	1.00
Head Phantom #2	PSNR (dB)	High-Energy	41.91	49.85	49.85	56.60	56.57
		Low-Energy	39.64	47.57	47.55	56.31	56.48
	SSIM	High-Energy	0.82	0.98	0.98	1.00	1.00
		Low-Energy	0.76	0.97	0.97	1.00	1.00
		Inter-Spectral	0.59	0.95	0.96	1.00	1.00

3.2. Study of digital phantoms

Figure 5 summarizes reconstructed DECBCT images in different views of the digital phantoms. The results using FDK, iterative reconstruction, and TV-regularized iterative reconstruction show severe LA artifacts. The proposed method achieves efficient LA artifact reduction, and no visible distortion is observed in the results. We did not perform the proposed method with additional TV regularization because the simulated LA-DECBCT scans are noiseless.

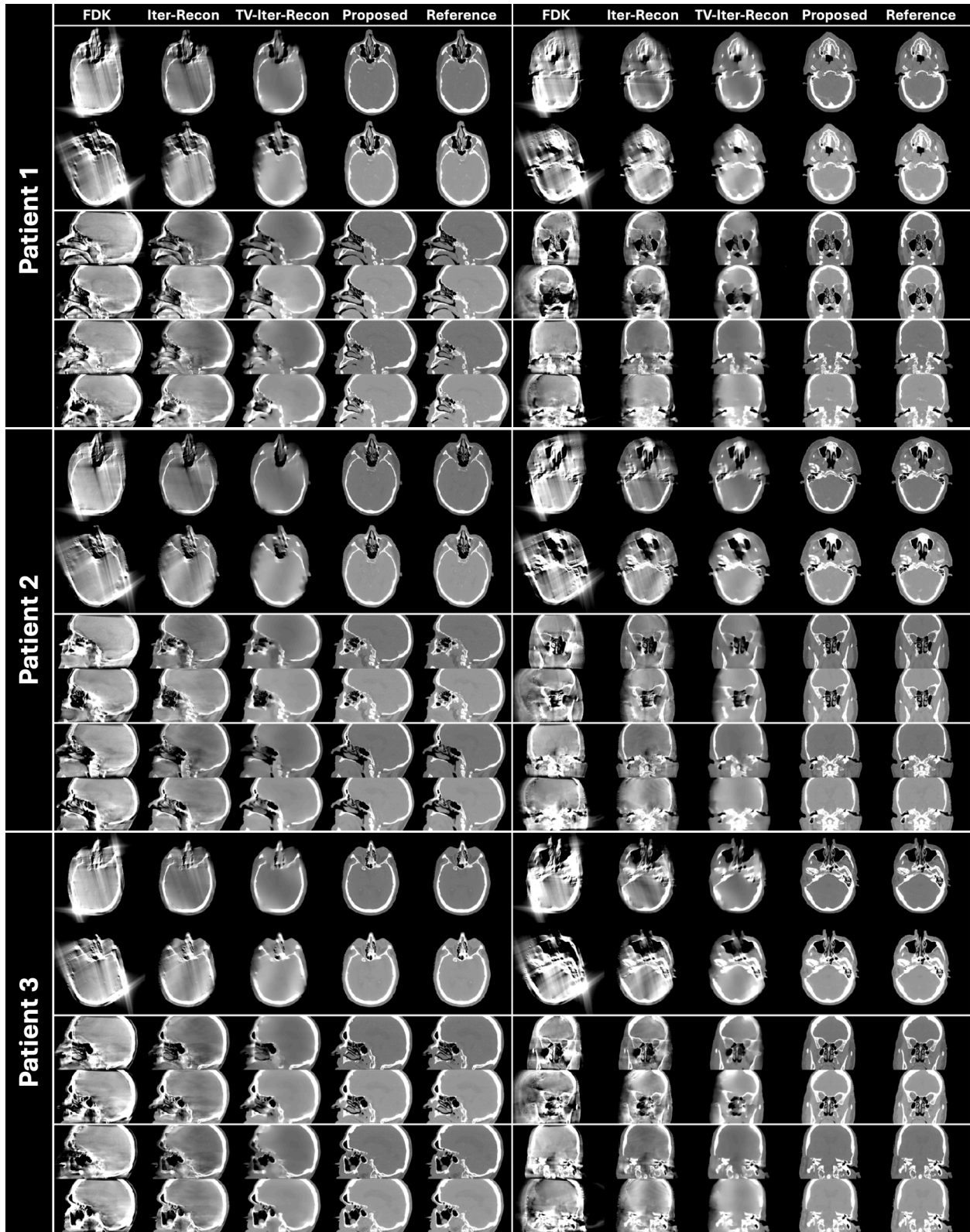


Figure 5. Reconstructed LA-DECBCT images of the digital phantoms using different methods. TV regularization is excluded in the proposed method in this digital phantom study. Display windows are [-750 - 250] HU for the FDK results and [-500 500] HU for the other results.

Table VI summarizes the quantitative analysis results of the digital phantom study. The MAE is computed within the body mask. All the metrics are calculated for each slice, and the means and standard deviations are computed from all the 450 values.

Table VI. Quantitative analysis of the digital phantom study. The inter-spectral SSIM is calculated between reconstructed high- and low-energy images. Other results are calculated between the reconstructed and reference images.

		FDK	Iter-Recon	TV-Iter-Recon	Proposed
MAE (HU)	High-Energy	419.34±57.80	100.52±27.33	92.25±19.45	14.42±2.37
	Low-Energy	591.08±67.14	149.44±31.99	131.27±30.17	19.94±3.16
PSNR (dB)	High-Energy	43.07±0.42	54.01±2.06	54.04±1.69	69.88±0.96
	Low-Energy	42.34±0.46	49.66±1.14	50.16±1.20	53.16±0.80
SSIM	High-Energy	0.84±0.01	0.99±0.00	0.99±0.00	1.00±0.00
	Low-Energy	0.80±0.02	0.98±0.01	0.99±0.00	1.00±0.00
	Inter-Spectral	0.64±0.05	0.98±0.01	0.98±0.00	1.00±0.00

4. Discussion

This work presents a practical solution to image reconstruction in LA-DECBCT. By enforcing the inter-spectral structural similarity constraint between DECBCT images during the optimization-based image reconstruction, LA artifacts are efficiently reduced in the reconstructed images. Compared to previously reported optimization-based methods, the proposed method eliminates the X-ray spectra measurement and the intensive computation for one-step material decomposition. Compared to the deep learning-based methods, the proposed method does not require paired DECBCT data for model training.

The similarity-based regularization has been introduced into iterative CT reconstruction to relax the data acquisition requirement of DECT for a long time. The main idea of these works is based on PICCS reconstruction, which obtains a prior image with accurate anatomical structures and enforces the constraint in similarity between the target image and the prior image during the subsequent iterative reconstruction. In Ref,²¹ a prior spectrally average CT is reconstructed from the slow kVp-switching projection data and used for target DECT reconstruction from sparse-view data. In Ref,⁴⁰ a prior high-energy CT is reconstructed from full-sampled data and used for similarity-based regularization in the target low-energy CT reconstruction from sparse-view data. In Ref,²² the size of low-energy projection data is two times more than that of high-energy data to obtain a prior low-energy CT, which is used for subsequent target high-energy CT reconstruction. In Ref,¹⁶ a prior image is reconstructed from the mixed-spectra data via exploiting Edholm's relationship in the Fourier decomposition of projection data.^{41,42} The prior image loses the DE spectral information and is used for similarity-based regularization in target DECT reconstruction. However, all these methods cannot work in LA-DECBCT because the prior image cannot be reconstructed from the acquired projection data at fidelity. In this work, we eliminate the reconstruction of the prior image and directly enforce the structural similarity between target DE images, enabling efficient image reconstruction in LA-DECBCT. This is the key novelty of the methodology in this work.

One advantage of the previously reported optimization-based one-step DTV algorithms over the proposed algorithm is that they can be extended to more challenging data acquisition schemes where the total angular coverage does not meet Tuy's data sufficiency condition.^{29,31,32} The success of the inter-spectral structural similarity regularization in this work relies on the acquisition of complete anatomical structures. Therefore, the total coverage of high- and low-energy projection views cannot be less than a short scan in the proposed work.

Incorporation of the DTV regularization into the proposed image reconstruction framework may address this issue and enable our method in more imaging applications, including faster scans for motion management, lower radiation dose, and avoidance of possible collisions between the gantry and the subject to be imaged. Of note, the integration of DTV will not affect the practicality of our method because the one-step material decomposition is not employed in the proposed algorithm. This will be the focus of our follow-up studies.

The deep learning-based DECBCT also has the aforementioned advantage over the proposed method.²⁷ In principle, the deep learning-based image prior can provide more information than the mathematically explicit image prior. As emphasized in the introduction, the major bottleneck of deep learning-based methods is the data pair requirement for supervised model training. Therefore, another focus of our future studies is to develop unsupervised alternatives to the existing models, which would pave the way for clinical applications of the deep learning-based LA-DECBCT. In our follow-up studies, we will investigate how to incorporate the proposed optimization-based image reconstruction into the deep learning methods for unsupervised enforcement of projection data consistency.

5. Conclusions

In this work, we propose an optimization-based image reconstruction regularized with inter-spectral structural similarity for LA-DECBCT. The proposed method can efficiently reduce LA artifacts during the image reconstruction, enabling quantitative DECBCT with comparable data acquisition time and radiation dose to that of a single-energy scan on current onboard scanners without hardware modification. This work is of great clinical significance and can boost the clinical application of DECBCT in image-guided radiation therapy and surgical interventions.

Acknowledgment

This research is supported in part by the National Institutes of Health under Award Number R01CA272991, R01EB032680, R01DE033512, P30CA008748 and U54CA274513.

References

1. Toepker M, Kuehas F, Kienzl D, et al. Dual energy computerized tomography with a split bolus—a 1-stop shop for patients with suspected urinary stones? *The Journal of urology*. 2014;191(3):792-797.
2. Graser A, Johnson TR, Hecht EM, et al. Dual-energy CT in patients suspected of having renal masses: can virtual nonenhanced images replace true nonenhanced images? *Radiology*. 2009;252(2):433-440.
3. Zhang L-J, Peng J, Wu S-Y, et al. Liver virtual non-enhanced CT with dual-source, dual-energy CT: a preliminary study. *European radiology*. 2010;20:2257-2264.
4. Yu L, Leng S, McCollough CH. Dual-energy CT-based monochromatic imaging. *American journal of Roentgenology*. 2012;199(5_supplement):S9-S15.
5. Buerke B, Wittkamp G, Seifarth H, Heindel W, Kloska SP. Dual-energy CTA with bone removal for transcranial arteries: intraindividual comparison with standard CTA without bone removal and TOF-MRA. *Academic radiology*. 2009;16(11):1348-1355.
6. Chandarana H, Megibow AJ, Cohen BA, et al. Iodine quantification with dual-energy CT: phantom study and preliminary experience with renal masses. *American Journal of Roentgenology*. 2011;196(6):W693-W700.
7. Jaffray DA, Siewerdsen JH, Wong JW, Martinez AA. Flat-panel cone-beam computed tomography for image-guided radiation therapy. *International Journal of Radiation Oncology* Biology* Physics*. 2002;53(5):1337-1349.
8. Siewerdsen J, Moseley D, Burch S, et al. Volume CT with a flat-panel detector on a mobile, isocentric C-arm: pre-clinical investigation in guidance of minimally invasive surgery. *Medical physics*. 2005;32(1):241-254.
9. Maybody M, Stevenson C, Solomon SB. Overview of navigation systems in image-guided interventions. *Techniques in vascular and interventional radiology*. 2013;16(3):136-143.
10. Roeske JC, Mostafavi H, Haytmyradov M, et al. Characterization of markerless tumor tracking using the on-board imager of a commercial linear accelerator equipped with fast-kV switching dual-energy imaging. *Advances in radiation oncology*. 2020;5(5):1006-1013.
11. Müller K, Datta S, Ahmad M, et al. Interventional dual-energy imaging—Feasibility of rapid kV-switching on a C-arm CT system. *Medical physics*. 2016;43(10):5537-5546.
12. Zbijewski W, Gang G, Xu J, et al. Dual-energy cone-beam CT with a flat-panel detector: Effect of reconstruction algorithm on material classification. *Medical physics*. 2014;41(2):021908.
13. Men K, Dai J, Chen X, Li M, Zhang K, Huang P. Dual-energy imaging method to improve the image quality and the accuracy of dose calculation for cone-beam computed tomography. *Physica Medica*. 2017;36:110-118.
14. Skaarup M, Edmund JM, Dorn S, Kachelriess M, Vogelius IR. Dual-energy material decomposition for cone-beam computed tomography in image-guided radiotherapy. *Acta Oncologica*. 2019;58(10):1483-1488.
15. Freixas GV. *Dual-energy cone-beam CT for proton therapy*. Université de Lyon; 2017.
16. Cho S, Lee S, Lee J, et al. A novel low-dose dual-energy imaging method for a fast-rotating gantry-type CT scanner. *IEEE Transactions on Medical Imaging*. 2020;40(3):1007-1020.
17. Cassetta R, Lehmann M, Haytmyradov M, et al. Fast-switching dual energy cone beam computed tomography using the on-board imager of a commercial linear accelerator. *Physics in Medicine & Biology*. 2020;65(1):015013.
18. Shi L, Lu M, Bennett NR, et al. Characterization and potential applications of a dual-layer flat-panel detector. *Medical physics*. 2020;47(8):3332-3343.
19. Wang W, Ma Y, Tivnan M, et al. High-resolution model-based material decomposition in dual-layer flat-panel CBCT. *Medical physics*. 2021;48(10):6375-6387.
20. Lee D, Lee J, Kim H, et al. A feasibility study of low-dose single-scan dual-energy cone-beam CT in many-view under-sampling framework. *IEEE transactions on medical imaging*. 2017;36(12):2578-2587.
21. Szczykutowicz TP, Chen G-H. Dual energy CT using slow kVp switching acquisition and prior image constrained compressed sensing. *Physics in Medicine & Biology*. 2010;55(21):6411.
22. Petrongolo M, Zhu L. Single-scan dual-energy CT using primary modulation. *IEEE transactions on medical imaging*. 2018;37(8):1799-1808.

23. Peng J. Single-scan half-fan DECT using static detector modulation: a preliminary study. *SPIE*; 2022:756-763.
24. Xiang J, Mao A, Xie J, et al. DER-GAN: Dual-Energy Recovery GAN for Conebeam CT. *IEEE Transactions on Computational Imaging*. 2023;
25. Peng J, Chang C-W, Qiu RL, et al. Diffusion model-based single-scan dual-energy cone-beam CT using primary beam splitting. *SPIE*; 2024:618-623.
26. Cao W, Shapira N, Maidment A, Daerr H, Noël PB. Hepatic dual-contrast CT imaging: slow triple kVp switching CT with CNN-based sinogram completion and material decomposition. *Journal of Medical Imaging*. 2022;9(1):014003-014003.
27. Zhang Y, Hu D, Yan Z, et al. TIME-Net: Transformer-integrated multi-encoder network for limited-angle artifact removal in dual-energy CBCT. *Medical Image Analysis*. 2023;83:102650.
28. Peng J, Chang C-W, Qiu RL, et al. Dual-Energy Cone-Beam CT Using Two Complementary Limited-Angle Scans with A Projection-Consistent Diffusion Model. *arXiv preprint arXiv:240311890*. 2024;
29. Chen B, Zhang Z, Xia D, Sidky EY, Pan X. Prototyping optimization-based image reconstructions from limited-angular-range data in dual-energy CT. *Medical Image Analysis*. 2024;91:103025.
30. Jiang X, Fang C, Hu P, Cui H, Zhu L, Yang Y. Fast and effective single-scan dual-energy cone-beam CT reconstruction and decomposition denoising based on dual-energy vectorization. *Medical physics*. 2021;48(9):4843-4856.
31. Chen B, Zhang Z, Sidky EY, Xia D, Pan X. Image reconstruction and scan configurations enabled by optimization-based algorithms in multispectral CT. *Physics in Medicine & Biology*. 2017;62(22):8763.
32. Chen B, Zhang Z, Xia D, Sidky EY, Pan X. Algorithm-enabled partial-angular-scan configurations for dual-energy CT. *Medical physics*. 2018;45(5):1857-1870.
33. Hsieh J. Computed tomography: principles, design, artifacts, and recent advances. 2003;
34. Rudin LI, Osher S, Fatemi E. Nonlinear total variation based noise removal algorithms. *Physica D: nonlinear phenomena*. 1992;60(1-4):259-268.
35. Wang Z, Bovik AC, Sheikh HR, Simoncelli EP. Image quality assessment: from error visibility to structural similarity. *IEEE transactions on image processing*. 2004;13(4):600-612.
36. Parker DL. Optimal short scan convolution reconstruction for fan beam CT. *Medical physics*. 1982;9(2):254-257.
37. Punnoose J, Xu J, Sisniega A, Zbijewski W, Siewerdsen J. spektr 3.0—A computational tool for x-ray spectrum modeling and analysis. *Medical physics*. 2016;43(8Part1):4711-4717.
38. Siddon RL. Fast calculation of the exact radiological path for a three-dimensional CT array. *Medical physics*. 1985;12(2):252-255.
39. Kingma DP. Adam: A method for stochastic optimization. *arXiv preprint arXiv:1412.6980*. 2014;
40. Wang T, Zhu L. Dual energy CT with one full scan and a second sparse-view scan using structure preserving iterative reconstruction (SPIR). *Physics in Medicine & Biology*. 2016;61(18):6684.
41. Edholm PR, Lewitt RM, Lindholm B. Novel properties of the Fourier decomposition of the sinogram. *SPIE*; 1986:8-18.
42. Mazin SR, Pelc NJ. Fourier properties of the fan-beam sinogram. *Medical physics*. 2010;37(4):1674-1680.